INORGANIC CHEMISTRY FRONTIERS

RESEARCH ARTICLE

View Article Online
View Journal | View Issue

Cite this: *Inorg. Chem. Front.*, 2026, **13**, 2912

A wireless gas sensing system enabling real-time seafood freshness monitoring based on Ru-In_2O_3 microtubes with dual-enhanced sensitivity and selectivity

Xue-Zhi Song, *[a] Yuxiang Chen,[a] Jintao Zhao,[a] Dekun Liu,[a] Ziwei Lv,[a] Yueying Wang,[a] Zhaonan Zuo,[a] Yu-Lan Meng,[a] Fei Li,*[b] Xiao-Feng Wang *[a] and Zhenquan Tan *[a]

The growing demand for seafood safety necessitates smart sensors with real-time monitoring capability for the biomarker triethylamine (TEA). However, it still faces tremendous challenges due to the limited sensitivity and selectivity of the sensing material. This study develops a topological transformation from a Ru-MIL-68 precursor to a Ru-doped In_2O_3 hollow hexagonal prism. These structural merits, including hierarchical porosity, uniform Ru dispersion, and abundant oxygen vacancies, endow this material with enhanced gas adsorption-diffusion kinetics and surface reactivity. The optimized Ru-In_2O_3-0.8 sensor exhibits exceptional TEA sensing performance: ultrahigh response (R_a/R_g = 493–100 ppm), fast recovery (τ_{rec} = 22 s), and a low detection limit (LOD = 11.3 ppb). Density functional theory calculations delineate that TEA binds preferentially to the Ru-In_2O_3 surface with a much larger adsorption energy than that of TEA on bare In_2O_3 or other gas molecules on Ru-In_2O_3, supporting the enhanced sensitivity and selectivity achieved by introducing Ru. Furthermore, a smart gas sensing system based on the Ru-In_2O_3-0.8 material demonstrates a real-time half-fin anchovy freshness monitoring application on mobile phones. This work not only proposes the structural modulations for exploration of advanced sensing materials but also guides the potential for real-time analysis, monitoring and diagnosis.

Received 27th November 2025,
Accepted 9th January 2026

DOI: 10.1039/d5qi02410b

rsc.li/frontiers-inorganic

1. Introduction

Food safety insurance is of paramount importance since it is directly related to public health. In particular, seafoods, such as fish and shrimp, face inevitable risks of meat spoilage due to their rich protein content during production, storage and transportation processes.[1,2] As seafood spoils, volatile amines, such as triethylamine (TEA), are released by the decomposition of amino acids or proteins due to the dramatically increased microbial activity.[3] During the early stages of spoilage, TEA release becomes detectable. According to recommendations from the European Commission and the American Conference of Governmental Industrial Hygienists (ACGIH), the permissible exposure limit for triethylamine in air is 1 ppm.[4] Therefore, the emitted TEA gas as an indicator of the freshness of seafood needs to be detected. The conventional methods, such as gas chromatography spectrometry, mass spectrometry and others, are limited by the precise sample pre-treatment, high equipment costs, prolonged analysis (>2 hours) and the requirement of well-trained operators.[5,6] Moreover, these methods cannot meet the requirements of real-time analysis and portable devices for applications in cold-chain logistics. Therefore, to negotiate these obstacles, it is essential to develop portable smart gas sensors and simultaneously explore advanced sensing materials for real-time food freshness monitoring. A smart gas sensor, also called an intelligent gas sensor, is a systematic module that is composed of the centered sensing unit, transducer unit, communication unit and other complementary parts.[7] In this context, the miniaturization of self-powered gas sensing devices and their integration with smartphones will provide an acceptable method for monitoring the seafood quality. Moreover, the performance of smart gas sensors relies greatly on the sensing materials, in which accessible sites, facile gas diffusion and reaction are in demand.

[a]*School of Chemical Engineering, Ocean and Life Sciences, School of General Education, Leicester International Institute, State Key Laboratory of Fine Chemicals, Dalian University of Technology, 2 Dagong Road, Liaodongwan New District, Panjin, Liaoning 124221, China. E-mail: songxz@dlut.edu.cn, wangxf@dlut.edu.cn, tanzq@dlut.edu.cn*

[b]*Medical Oncology Department of Thoracic Tumors, Liaoning Cancer Hospital & Institute, Cancer Hospital of Dalian University of Technology, Shenyang 110042, Liaoning, China. E-mail: lifei@cancerhosp-ln-cmu.com*

Indium oxide (In_2O_3), as a typical n-type semiconducting metal oxide, has gained intensive attention in the gas sensing field due to its low production cost, facile fabrication, excellent conductivity and outstanding chemical stability.[8–11] Nevertheless, the majority of pure or bulk In_2O_3 based materials usually suffer from unsatisfactory sensitivity and selectivity at a low working temperature, not meeting the requirement of seafood freshness insurance. As a consequence, it is imperative to improve their gas sensing performance by nanostructure engineering, electronic modulation, chemical sensitization and defect engineering. (i) Nanostructure engineering: the morphologies are related to the gas transportation, the exposed active sites and the receptor function, greatly affecting the sensing performance. Up to now, diverse nanostructures have been explored, such as nanoparticles, one-dimensional nanowires, and two-dimensional nanosheets.[12–16] In particular, hollow structures, such as micro-spherical and tubular morphologies with porous walls, have demonstrated great promise for superior gas sensing performance due to their good surface permeability, high specific surface area and ample exposed sites on the inner and outer surfaces.[17]

(ii) Electronic modulation: the sensing performance is greatly affected by the electronic band structure, since it may lead to surface active species, carrier concentration and transfer optimization. The heterojunctions with an intimate interfaces are powerful tools to regulate the electronic structure due to the work function difference. For instance, various secondary semiconductive metal oxides have been integrated with In_2O_3 to fabricate p–n heterojunctions, such as NiO/In_2O_3 as a formaldehyde gas sensor and $NiCo_2O_4$–In_2O_3 and Co_3O_4–In_2O_3 for TEA sensing.[18,19] Specifically, the $NiCo_2O_4$–In_2O_3 sensor exhibits an 8.3-fold increase of response value (550 at 100 ppm TEA) compared to that of bare In_2O_3 due to the adjusted carrier transfer process and other synergies. Its selectivity needs to be further improved.[20,21]

(iii) Chemical sensitization: anchoring another active component onto In_2O_3 will additionally facilitate surface gas sensing reactions. Loading CuO with a strong chemical affinity for H_2S on In_2O_3 porous nanosheets showed a lower limit of detection and superior selectivity. To be notable, noble metal units usually realize chemical sensitization according to gas molecule dissociation and catalytic activation effects.[22] In recent years, ruthenium (Ru) has been widely employed due to its excellent electronic sensitization effect on metal oxides and its ability to enhance gas sensing performance. Qiao *et al.* found that Ru dopants significantly reduce the activation energy for TEA oxidation (from 71.12 kJ mol^{-1} to 29.39 kJ mol^{-1}), accelerating reaction kinetics, and inducing oxygen vacancies and forming Schottky junctions with In_2O_3, narrowing its bandgap and optimizing carrier concentration.[23] Co-doping Ru and Mo in Co_3O_4 further enhances oxygen vacancy concentration and lowers the optimal operating temperature to 160 °C.[24] Xu's group utilized Ru-based alloys to strengthen target gas interactions and stabilize amorphous active phases.[25]

(iv) Defect engineering: precise control of intrinsic oxygen vacancy concentration in metal oxides would simultaneously optimize the electronic structure and surface active sites. As electron donors, oxygen vacancies narrow the bandgap (*e.g.*, SnO_2 from 3.83 eV to 3.52 eV), increase carrier concentration, and accelerate adsorbed oxygen ionization, thereby enhancing gas response. For instance, oxygen-deficient SnO_2 (29.47% O_V) exhibits a doubled response to 6 ppm H_2 (2.3 *vs.* 1.13 of pristine SnO_2) with a detection limit of 0.1 ppm. Similarly, black-phase In_2O_3 (B-In_2O_3) with 44.2% oxygen vacancies shows significantly improved room-temperature NO_2 response due to synergistic enhancement of gas adsorption and electron transfer. This strategy provides a novel approach for overcoming the limitations of conventional heterojunction/noble metal modification by directly regulating intrinsic defects.[26,27] Moreover, notwithstanding the above achievements, it is still in the early stage of simultaneously implementing the above-mentioned structural design aspects to enhance the sensitivity and selectivity, and the underlying mechanism is still unclear.

Metal–organic frameworks (MOFs) have been utilized as precursors to fabricate multifunctional materials. The different metal centers with atomical homogeneity enable the homogenously distributed components and the corresponding strong interaction.[28] Furthermore, the morphologies of pristine MOFs would be preserved and even converted into hollow structures during structure transformation. These above merits enable the fabrication of various materials in our previous work, such as single-atom Ce site within the Cu/MoO_2@C matrix, multi-shelled Ln-doped CoP/CoO microspheres and triple-shelled ZnO/$ZnFe_2O_4$ heterojunctional hollow microspheres as sensing materials.[29–31] Therefore, introducing an appropriate functional unit into In-based MOFs at the source can effectively form hollow structures and leverage the promoting effects induced by functional motifs.

As proof-of-concept research, this work proposes bimetallic MOFs (Ru-MIL-68) as precursors to fabricate hollow hexagonal Ru-In_2O_3 microtubes. The confinement effect within bimetallic Ru-MIL-68 ensures uniform Ru dispersion to strengthen the Ru-In_2O_3 interaction and modulate the electronic structure. The structural merits, including hollow nanostructure engineering, Ru-induced electronic band structure regulation and chemical sensitization effects, synergistically enhance the sensitivity and selectivity, supported by systematic experimental and theoretical investigations. The Ru-In_2O_3-0.8 based sensor with an optimal Ru concentration shows an impressively high response value of 493 at 100 ppm TEA and high selectivity coefficients. The smart gas sensing system further demonstrates practical potential in real-time monitoring of seafood freshness.

2. Experimental details

2.1. Synthesis of Ru-In_2O_3 materials

Ru-MIL-68(In) was synthesized by modifying a solvothermal method. $In(NO_3)_3{\cdot}4H_2O$ (186.4 mg, 0.5 mmol) and H_2BDC

(50.0 mg, 0.3 mmol) were dissolved in DMF (30 mL) and sonicated for 5 min. Then, a certain amount of $RuCl_3$ (0.83 mg, 0.004 mmol) was added to the mixed solution and stirred for 10 min. The uniform solution was transferred into an 80 mL autoclave, heated to 100 °C, and kept at this temperature for 4 h. After natural cooling to room temperature, the brown precipitate was collected by centrifugation, washed several times with ethanol, and then dried at 60 °C for 12 h. Thus, the bimetallic Ru(0.8%)-MIL-68 precursors were obtained. The Ru/In molar ratios were precisely controlled at 0.4% and 1.6% by adjusting the amount of $RuCl_3$ (0.415 mg and 1.66 mg) added during synthesis, leading to the formation of Ru(0.4%)-MIL-68 and Ru(1.6%)-MIL-68 materials.

The resultant Ru(x%)-MIL-68 precursors were heated at 450 °C for 3 h at a heating rate of 2 °C min^{-1} in a muffle furnace, resulting in the formation of Ru-In_2O_3 powders, denoted as Ru-In_2O_3-0.4, Ru-In_2O_3-0.8 and Ru-In_2O_3-1.6. For the synthesis of the compared In_2O_3 material, the precursor of MIL-68 was adopted for thermal treatment, which was initially prepared by adding only $In(NO_3)_3{\cdot}4H_2O$ without Ru doping modification.

2.2. Fabrication and measurement of the gas sensor

The gas-sensitive devices were fabricated according to the following standardized protocol. Sensing materials were homogenized *via* mechanical grinding in ethanol to form a uniform suspension, which was subsequently applied onto the exterior of alumina substrates (equipped with dual Au electrodes and an integrated heating filament). Gas response evaluations were conducted using a commercial CGS-8 analytical platform (Beijing Elite Technology Co., Ltd, Beijing, China), with system configuration schematics provided in Fig. S1. For n-type semiconductor sensors, the response value was calculated as R_a/R_g, where R_a and R_g denote resistances in ambient air and analyte gas, respectively. All measurements were performed under controlled humidity conditions (50% RH) unless explicitly varied.

2.3. Fabrication of the smart wireless TEA sensor and fish freshness tests

The smart TEA sensing system based on the STM32F103C8T6 microcontroller was utilized to assess the gas sensing performance. The analog signal of the dynamic change of the resistance (R_S) of the sensing material caused by gas concentration was converted into a digital signal through the Analog-to-Digital Converter (ADC), and the digital signal was the voltage data (V_{RL}) collected by the ADC. The details are included in the SI.

A 100 g sample of fresh half-fin anchovy was hermetically sealed in a 1 L beaker at a room temperature of 30 °C and relative humidity of 50%. Subsequently, 50 mL of headspace gas was extracted from the beaker at regular intervals and injected into a 20 L sealed container, and the smart gas sensor was used to detect the concentration of TEA gas.

2.4. DFT calculations

The adsorption energies and charge density difference were determined using the DMol3 program package in Materials Studio. The exchange and correlation terms were determined using the Generalized Gradient Approximation (GGA) in the form proposed using the Perdew–Burke–Ernzerhof (PBE) formulation. The self-consistent calculations applied a convergence energy threshold of 10^{-5} eV. The adsorption of TEA, EtOH, acetone, hexane and *n*-PrOH on the In_2O_3 (222) or Ru–In_2O_3 (222), and the adsorption between sensing materials and target gas were investigated in this work. In surface adsorption models, a vacuum layer of about 20 Å was added in the *Z*-direction of the slab model to avoid the effects of periodic boundary conditions. The binding energies are calculated with the following equation: $E_{ads} = E_{A+B} - E_A - E_B$, where E_{ads}, E_{A+B}, E_A and E_B are the energy of adsorption, the total energy of In_2O_3 (222) or Ru–In_2O_3 (222) with the adsorbing target gas, the total energy of In_2O_3 (222) or Ru-In_2O_3 (222), and the total energy of the individual target gas molecule, respectively. The isosurface level of charge density difference of In_2O_3 (222) or Ru–In_2O_3 (222) with the adsorbing target gas was 0.02 e $Å^{-3}$. The saturation level of the 2D display of charge density difference was set from −0.01 to 0.02 e $Å^{-3}$.

3. Results and discussion

3.1. Synthesis, structure and characterization studies

The fabrication process of Ru-In_2O_3 microtubes is illustrated in Fig. 1. Firstly, one-pot synthesis of Ru^{3+} and In^{3+} involved bimetallic MOFs was achieved under solvothermal conditions. Secondly, the bimetallic MOFs were thermally treated to form the target Ru-In_2O_3 microtubes as sensing materials. The homogeneous introduction of Ru species within bimetallic MOFs is quite different from the well-documented stepwise loading of secondary noble metal or transition metal units.[20] This elaborate design would guarantee the highly dispersed Ru species at the atomic scale within In_2O_3, significantly contributing to the structural modulation and sensing ability.

Comprehensive structural characterization studies were conducted through scanning electron microscopy (SEM) to investigate the morphological evolution. Fig. 2a clearly illustrates the hexagonal prism morphology of Ru(0.8%)-MIL-68 with a size of 1–2 μm in length and 400–800 nm in width. Regardless of the feeding amount of Ru, the hexagonal prism morphology and the size are basically consistent in Ru(0.4%)-MIL-68, Ru(1.6%)-MIL-68 and bare MIL-68 (Fig. S2). After subsequent high-temperature calcination, the overall hexagonal configuration was maintained, while the distinctive hollow structures emerged in Ru-In_2O_3-0.8 microtubes, as evidenced by the SEM images in Fig. 2b and c. The unique hollow hexagonal prism architecture was further confirmed by the transmission electron microscopy (TEM) image (Fig. 2d). This hollow feature with ample pores on the walls offers dual functional advantages: the substantially increased specific surface area providing abundant active sites for gas molecule adsorp-

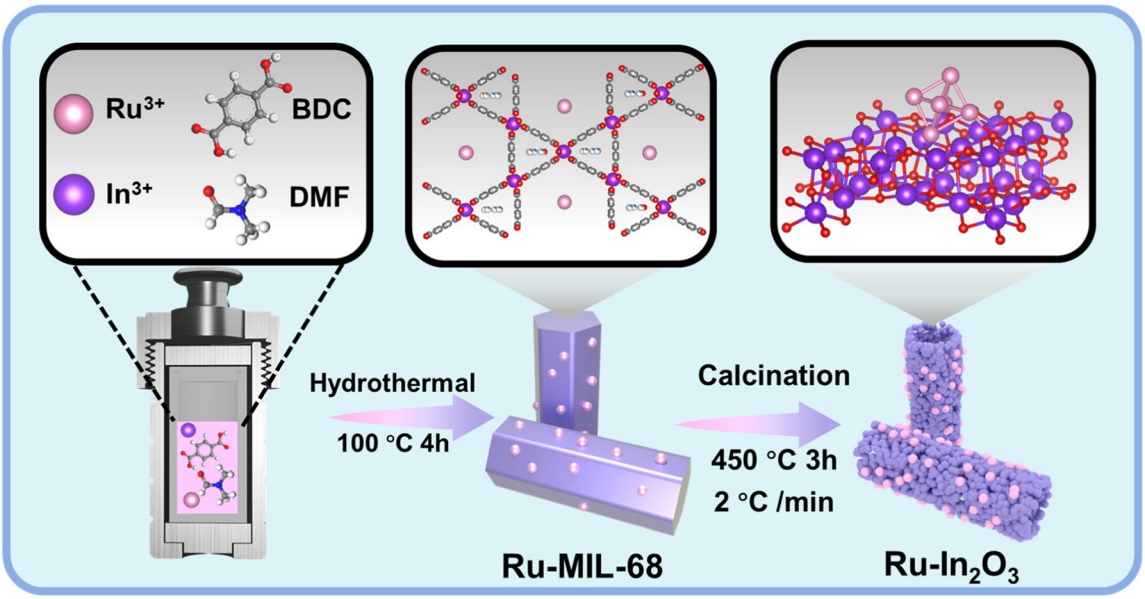

Fig. 1 Schematic illustration of the synthesis of Ru-In_2O_3 microtubes.

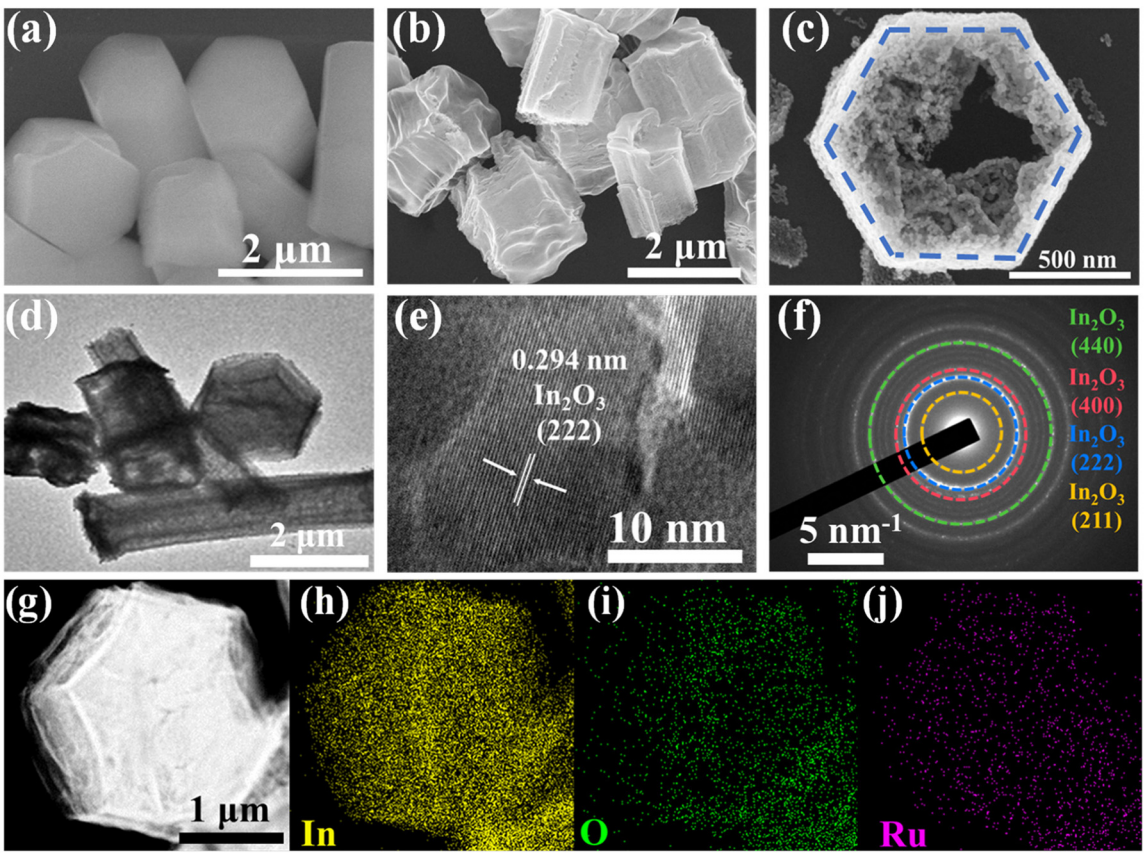

Fig. 2 SEM images: (a) Ru(0.8%)-MIL-68, and (b and c) Ru-In_2O_3-0.8; (d) TEM image, (e) HRTEM image and (f) SAED image of Ru-In_2O_3-0.8; (g) HAADF-STEM image; and (h–j) elemental mapping images of Ru-In_2O_3-0.8.

tion and the well-defined tubular channels facilitating rapid gas diffusion. The HRTEM image in Fig. 2e shows an interplanar distance of 0.294 nm, which corresponds to the (222) plane of cubic In_2O_3. This value is slightly larger than that of pristine In_2O_3 (0.292 nm), indicating a minor lattice expansion due to the substitution of Ru with In in the lattice. This result

further confirms that Ru was successfully introduced. In addition, this image also reveals that the walls of the hexagonal microtube are enveloped by a large number of small nanoparticles (about 35 nm), serving as critical sensing units. The diffraction rings in the corresponding SAED pattern confirm the existence of the cubic In_2O_3 phase (Fig. 2f). The TEM elemental mapping images show that In, O and Ru elements are uniformly distributed in the Ru-In_2O_3-0.8 microtubes, maximizing the modulation effect endowed by Ru functionality (Fig. 2h–k).

To characterize the crystal structure and phase composition of In_2O_3 and Ru-In_2O_3 powders, X-ray diffraction (XRD) analysis was employed. As shown in Fig. 3a, pristine In_2O_3 exhibited diffraction peaks at 21.5°, 30.6°, 35.5°, 51.0°, and 60.7°, corresponding to the (211), (222), (400), (440), and (622) planes of the cubic In_2O_3 phase (JCPDS No. 06-0416). After Ru species incorporation, the XRD patterns in Ru-In_2O_3 materials remain unchanged without any detectable diffraction peaks of Ru, which indicates that the Ru species does not induce any variation in the crystalline structure of In_2O_3 and its homogeneous distribution.[32] The surface elemental composition and oxidation states of In_2O_3 and Ru-In_2O_3 were further investigated by using X-ray photoelectron spectroscopy (XPS). The full-range XPS spectra presented in Fig. 3b provide clear evidence of the presence of Ru, O and In elements in the Ru-In_2O_3-0.8 material. As shown in Fig. 3c, the asymmetric peaks observed in the O 1s spectra can be precisely deconvoluted into three distinct peaks for bare In_2O_3 and Ru-In_2O_3-0.8 materials, corresponding to the lattice oxygen (O_L), the oxygen vacancies (O_V), and the surface absorbed oxygen (O_C). The higher O_V concentration in the Ru-In_2O_3-0.8 material critically influences the gas-sensing performance by providing more active sites for gas molecule adsorption and surface chemical reactions. Simultaneously, oxygen vacancies function as catalytic centers that lower the activation energy for gas-phase redox reactions, creating synergistic effects that enhance both surface reactivity and charge transfer efficiency. This dual functionality establishes oxygen vacancy engineering as a pivotal strategy for improving adsorption capacity and catalytic activity.[23,33,34]

The XPS analysis of In 3d core-level spectra (Fig. 3d) reveals distinct chemical environment modifications upon Ru incorporation. Bare In_2O_3 exhibits characteristic In $3d_{3/2}$ and In $3d_{5/2}$ peaks at 444.3 eV and 451.8 eV, respectively. After the introduction of Ru, both peaks shift toward higher binding energies.[35,36] The higher electronegativity of Ru (2.2) compared to In (1.78) may explain the binding energy shift and suggest electron transfer from In to Ru centers, confirming chemical interactions between In and Ru for gas sensing enhancement.[37] In general, the XPS spectrum of Ru 3d overlaps with the binding energy range of C 1s.[38] The additional characteristic peak of Ru $3d_{5/2}$ is still observed with binding energies of 281.9 eV, 281.0 eV and 280.0 eV, implying that the majority of the Ru species on the Ru-In_2O_3-0.8 can be assigned to $Ru^{\delta+}$($4 < \delta \leq 8$), Ru^{4+} and Ru^0, respectively (Fig. 3e and f).[25]

The N_2 adsorption–desorption isotherms of Ru-In_2O_3-0.8 exhibit characteristic Type IV isotherms, which is indicative of their mesoporous nature (Fig. S3). The Ru incorporation slightly increases the Brunauer–Emmett–Teller (BET) specific surface areas from 36.60 of In_2O_3 to 37.91 $m^2\ g^{-1}$ in the Ru-In_2O_3-0.8 material. The enlarged specific area can increase the contact effectivity and subsequent reaction between gas mole-

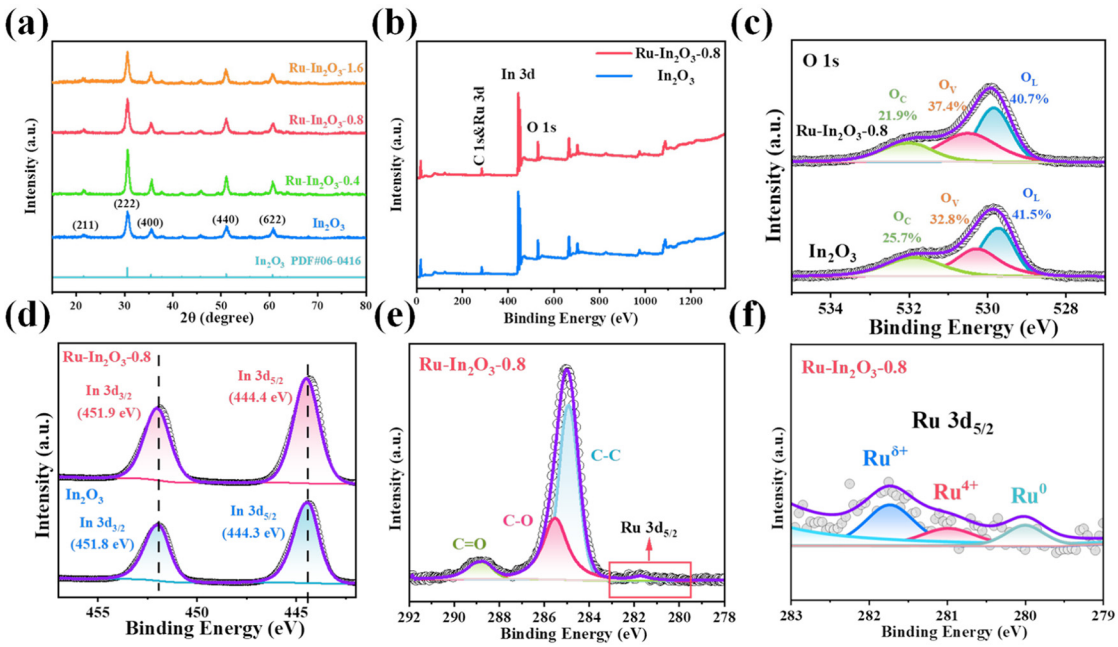

Fig. 3 (a) XRD patterns of pristine In_2O_3, Ru-In_2O_3-0.4, 0.8 and 1.6 samples. (b–f) Full, O 1s, In 3d, C 1s and Ru 3d and enlarged Ru 3d XPS spectra of In_2O_3 and Ru-In_2O_3-0.8, respectively.

cules and the sensing material surface, being conducive to the enhanced sensing performance.

3.2 Gas sensing properties

Encouraged by the unique microtube morphology with Ru species as an electronic or chemical structure modifier, the Ru-In_2O_3 based sensors were fabricated to investigate the sensing properties with bare In_2O_3 as a comparison. The In_2O_3 and Ru-In_2O_3 materials show decreased resistance upon increasing temperature, revealing the thermally excited charge carrier migration from valence to conduction bands (Fig. S4 and S5). Additionally, the resistance values of the Ru-In_2O_3 based sensor under an air atmosphere are much higher than those of the bare In_2O_3 counterpart at each temperature due to the formation of a Schottky barrier.[39] The enlarged baseline resistance values of Ru-In_2O_3-0.8 in air may provide the foundation for the improved response values for the n-type semiconductor.

Owing to the fact that the operating temperature greatly affects the sensing ability, the temperature-dependent gas sensing characteristics of In_2O_3 and Ru-In_2O_3 based sensors toward 100 ppm TEA vapor were systematically performed across the 100–200 °C operational window (Fig. 4a). All sensors demonstrate similar volcano-shaped profiles, with a gradual response growth followed by a falling tendency at a certain temperature. This non-monotonic behavior originates from competing thermal activation and molecular desorption processes: elevated temperatures initially enhance surface reaction kinetics by providing sufficient activation energy for analyte–oxygen species interactions, while excessive heating (>120 °C) accelerates molecule desorption rates beyond critical thresholds, significantly reducing gas–surface contact duration and response values. Meanwhile, the volcano-shaped response dependence on the Ru content suggests an optimal doping threshold (0.8 at%), potentially attributable to competing effects: enhanced active sites at lower concentrations *versus* Ru aggregation and electronic screening at higher loadings.[24,40,41] The Ru-In_2O_3-0.8 sensor demonstrates optimal performance at 120 °C with a remarkable response magnitude (R_a/R_g = 493) – 2.74-fold enhancement compared to pristine In_2O_3 (R_a/R_g =

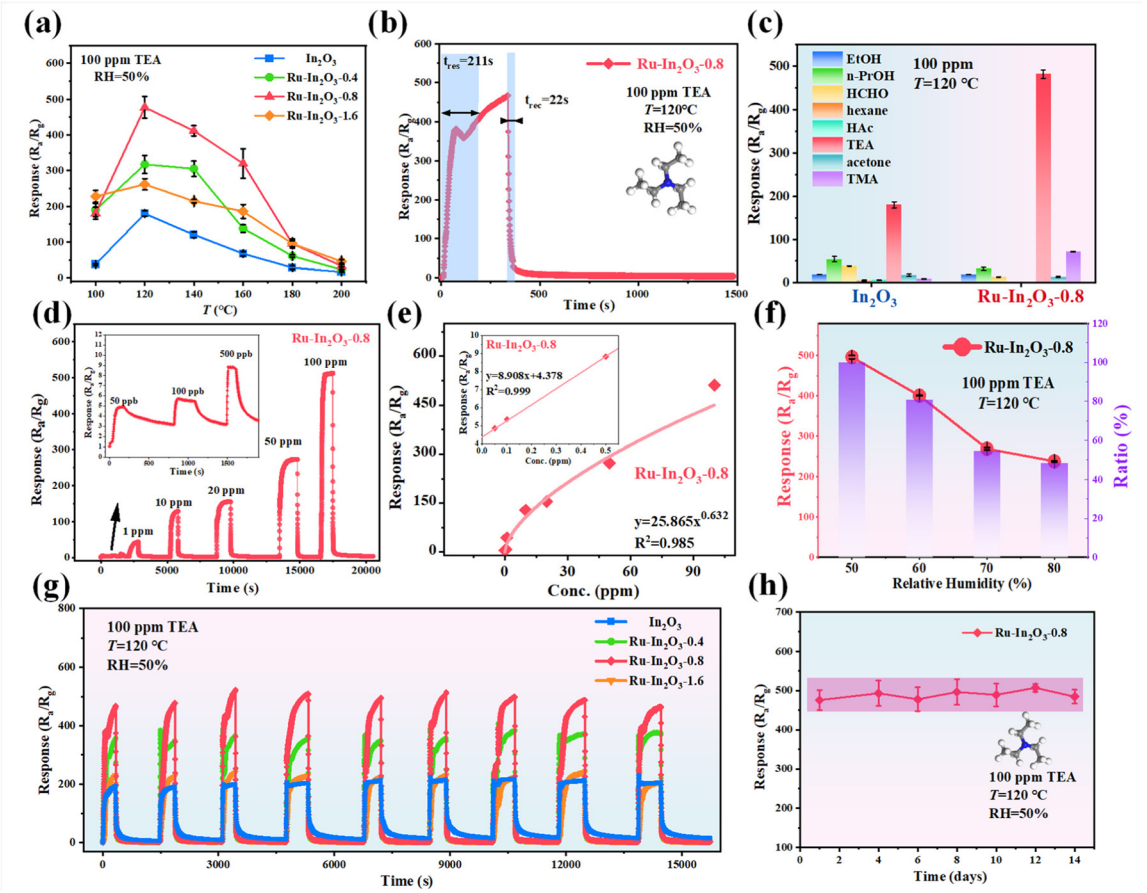

Fig. 4 (a) The response value of the sensors toward 100 ppm TEA gas at 100 °C–200 °C. (b) Response/recovery times of In_2O_3 and Ru-In_2O_3-0.8 sensors to 100 ppm TEA gas at 120 °C. (c) The response values of In_2O_3 and Ru-In_2O_3-0.8 sensors towards 100 ppm of various gases at 120 °C. (d) Dynamic response of the sensor based on Ru-In_2O_3-0.8 to 0.05–100 ppm TEA gas at 120 °C. (e) The corresponding linear regression fitting between response and TEA concentration. (f) The response values of the Ru-In_2O_3-0.8 sensor under different relative humidities. (g) Cycling stability of In_2O_3 and Ru-In_2O_3 sensors with different doping ratios to 100 ppm TEA gas at 120 °C. (h) Long-term stability of the Ru-In_2O_3-0.8 sensor to 100 ppm TEA gas at 120 °C.

180, Fig. S6). This temperature-specific response maximization results from balanced thermal energy input and adsorption–desorption equilibrium. The activation energy threshold of triethylamine precisely matches the catalytic ability of the Ru catalytic center.[4,42] Systematic evaluation of temperature-dependent response profiles establishes 120 °C as the optimal operational temperature, which was adopted for further investigations.

The dynamic sensing characteristics were quantitatively evaluated through response–recovery kinetic analysis. According to the standard protocol, the response time (τ_{res}) and recovery time (τ_{rec}) of the In_2O_3 sensor were determined to be 212 s and 176 s toward 100 ppm TEA at an optimal operation temperature (120 °C), revealing its sluggish response dynamics. The recovery time of Ru-In_2O_3-0.8 dramatically declined to 22 s, suggesting that the recovery kinetics were accelerated with an 8-fold improvement by Ru species (Fig. 4b and S6b). As illustrated in Fig. S7, for various interfering gases, the Ru-In_2O_3-0.8 sensor has the fastest recovery speed and a considerable response speed for TEA. The responsiveness of the In_2O_3 and Ru-In_2O_3-0.8 sensors to different gases at 100 ppm concentration was investigated and is compiled in Fig. 4c to evaluate the critical selectivity. The Ru-In_2O_3-0.8 sensor shows the highest response to TEA and minimal response values to other gases. The responses to EtOH (ethanol), *n*-PrOH (*n*-propanol), HCHO (formaldehyde), hexane, HAc (acetic acid), TEA, acetone and TMA (trimethylamine) are 19.8, 32.5, 13.4, 1.9, 1.85, 493, 14.1 and 71.5, respectively, indicating that the Ru-In_2O_3-0.8-based sensor exhibits superior selectivity to TEA gas (Fig. S8). Thorough observation reveals the selectivity enhancement of Ru-In_2O_3-0.8: the response to TEA is significantly improved, while its sensitivity toward most of other interfering gases is reduced to varying degrees compared to pristine In_2O_3. The quantitative evaluation and mechanistic investigation of outstanding selectivity enhancement will be elucidated through selectivity coefficients and theoretical calculations (*vide infra*).

The dynamic response–recovery characteristics of the Ru-In_2O_3-0.8-based sensor across a wide TEA concentration range (0.05–100 ppm) are shown in Fig. 4d. The near-rectangular response–recovery profiles indicate stable and reversible surface interactions. The sensor exhibits a rising trend of response values with an increased TEA concentration. The data in the 0.05–100 ppm range were fitted with a power function ($y = 25.865 \times x^{0.632}$), which accurately describes the trend of the response value tending towards saturation as the concentration increases. Linear regression analysis of the low-concentration regime (0.05–0.5 ppm) reveals an ultra-low limit of detection (LOD) of 11.3 ppb, which was estimated by using the equation LOD = $3*\sigma/S$ (the detailed calculation process is provided in the SI).[25] This demonstrates precise quantification capabilities for trace-level TEA detection (Fig. 4e). These collective features, including sub-ppm sensitivity, rapid recovery kinetics (τ_{rec} = 22 s) and robust performance across four orders of magnitude of concentration variation, highlight its potential for practical applications in marine product freshness assessment, where early spoilage detection at ppb-level TEA concentrations is critical.

Given the ubiquitous presence of moisture in real-world TEA detection environments, we rigorously evaluated the sensing ability and humidity tolerance of the Ru-In_2O_3-0.8 sensor under varying high relative humidity (RH) conditions. As depicted in Fig. 4h, the response values decreased to 81%, 54.5%, and 48.5% of the baseline (RH = 50%) at 60%, 70%, and 80% RH, respectively. This response performance degradation arises from the competitive adsorption of water molecules. The Ru-In_2O_3-0.8 sensor also maintained responsive kinetics even under humidity-induced effects (RH = 80%), with τ_{res}/τ_{rec} being 226 s/32 s, representing only 8.5% and 45.5% increases in response/recovery durations compared to those under low humidity. The preserved temporal performance may stem from oxygen vacancy-assisted water dissociation pathways, which mitigate moisture interference through enhanced surface desorption efficiency.[23,32]

All In_2O_3 and Ru-doped In_2O_3 sensors maintain quasi-rectangular response profiles across all cycles, with no observable signal attenuation or baseline drift. The Ru-In_2O_3-0.8 sensor demonstrated exceptional reproducibility (Fig. 4f), exhibiting a minimal response variation of ±2.1% (relative standard deviation) and consistent recovery kinetics (τ_{rec} = 22 ± 1.5 s) throughout testing. This TEA sensing performance consistency under alternative TEA/air exposure confirms robust structural integrity and stable surface reactivity, being one strong supportive parameter for practical sensing applications. The response values of the Ru-In_2O_3-0.8 sensor to 100 ppm TEA at different time intervals presented in Fig. 4g showed negligible changes over 14 days, indicating that the Ru-In_2O_3-0.8 sensor also has good long-term stability.

3.3. Gas sensing mechanism

A consistent rise in the baseline resistance of Ru-In_2O_3 materials was observed with increasing Ru doping concentration at constant temperature, attributable to the work function difference between Ru and In_2O_3. This interfacial electronic effect was quantitatively confirmed by UPS analysis (Fig. S10a and b), with a 0.13 eV increase in work function for Ru-In_2O_3-0.8. The underlying modulation of electrical properties resulting from Ru incorporation can be explained by electron transfer at the metal–semiconductor interface. Electrons transfer from In_2O_3 to the Ru dopants due to the higher work function of Ru, leading to the formation of charge-depleted regions and consequently an increase in overall resistance. This aligns with the electronic sensitization mechanism reported for noble metal/oxide systems, where work function mismatch induces electron transfer to the metal phase.[25] Mott–Schottky characterization (Fig. S11) confirmed the preserved n-type semiconductor behavior for both pure In_2O_3 and Ru-doped In_2O_3, as evidenced by positive slopes. Fig. 5a presents the complete energy band structure of In_2O_3 and Ru-In_2O_3-0.8. The band gaps of In_2O_3 and Ru-In_2O_3-0.8 are 3.25 eV and 3.17 eV, respectively, measured by UV-Vis spectra (Fig. S12a and b). The narrowed band gap of Ru-In_2O_3-

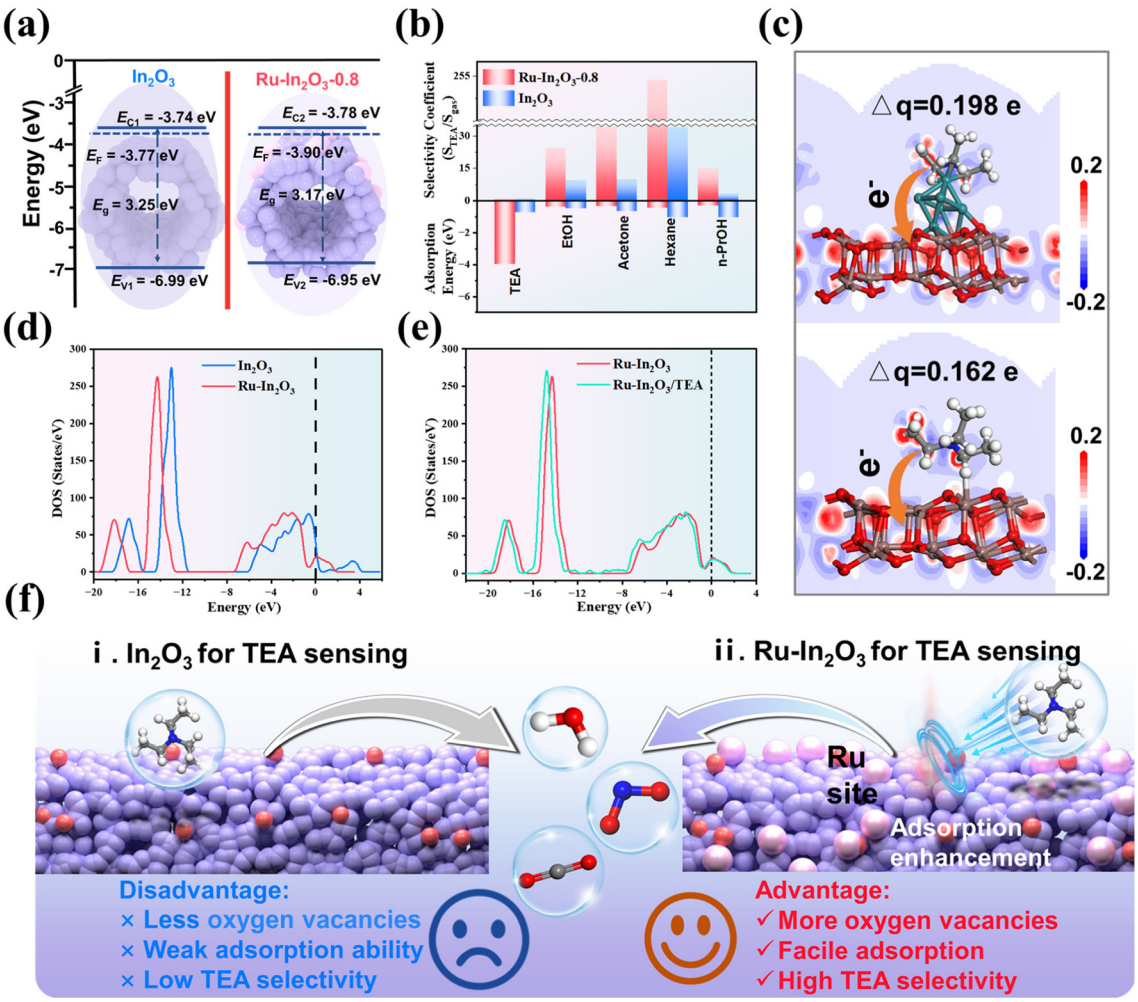

Fig. 5 (a) Schematic diagram of energy band changes of the In_2O_3 and Ru-In_2O_3-0.8 samples. (b) Selectivity coefficient and adsorption energy values of In_2O_3 and Ru-In_2O_3 under different gases. (c) Charge density difference graphs of TEA-adsorbed Ru-In_2O_3 and In_2O_3. The red atoms represent O, the brown atoms represent In, the green atoms represent Ru, the grey atoms represent C, the white atoms represent H and the blue atom represents N. Density of states (DOS) of (d) In_2O_3 and Ru-In_2O_3; and (e) TEA-adsorbed Ru-In_2O_3. (f) The advantages of TEA sensing over Ru-In_2O_3.

0.8 facilitates electron transitions and oxygen vacancy generation, which contributes significantly to the enhanced gas-sensing capabilities.[43] The decline of the Fermi level position (Ru-In_2O_3-0.8, −3.90 eV *vs.* pure In_2O_3, −3.77 eV) leads to a larger energy level difference with oxygen, which makes electron transfer between oxygen and the material easy and is also conducive to the increase of adsorbed oxygen.[44,45] An electron-enriched Ru state facilitates the adsorption and reaction of active oxygen species and TEA, thereby enhancing the overall gas response.[46,47]

The collective electrical analyses reveal that Ru doping effectively modulates carrier concentration through interfacial charge redistribution while maintaining fundamental n-type semiconductor characteristics, establishing a critical foundation for optimizing gas-sensing performance through electronic structure engineering. The sensing mechanism of the n-type In_2O_3-based TEA gas sensor could be explained by the electron depletion layer (EDL) model. It is well accepted that the resistance changes in the metal oxide sensing material are related to the adsorption and desorption of reductive gas molecules. As illustrated in Fig. S13, under an air atmosphere, Ru-In_2O_3 can adsorb oxygen molecules on its surface and oxygen molecules further react with movable electrons in the conduction band, leading to the formation of negative oxygen species (such as O_2^- and O^-) and a thick electron depletion region on the surface of Ru-In_2O_3. Therefore, the electrical resistance of the material is comparatively high.[48] When the sensing material comes in contact with TEA gas, O^- and O_2^- ions on the surface of the material would react with the gas to form NO_2, CO_2 and H_2O.[49,50] Electrons are simultaneously re-injected to the material's surface, resulting in a sharp decrease in the sensor's resistance (Fig. S5). Owing to the initial much higher resistance in air of Ru-In_2O_3-0.8 and a more active surface TEA sensing reaction, the resistance would decline to a very large degree, resulting in a larger response value and improved sensitivity. The selectivity coefficients (SC = R_{TEA}/

R_{gas}, Fig. 5b) of the pure In_2O_3-based sensor are calculated to be 9.4, 10.1, 34 and 3.3 relative to EtOH, acetone, hexane and *n*-PrOH. The Ru-In_2O_3-0.8-based sensor exhibits sustainably increased SC of 24.3, 34.2, 253.7 and 14.8 relative to the aforementioned gases. This quantitative selectivity coefficient evaluation demonstrates that Ru species also delivers pronounced selectivity improvement.

To gain a deeper insight into the impact of Ru doping on the improved sensing selectivity, density functional theory calculations (DFT) were employed to examine the adsorption features of different gas molecules on the surface of In_2O_3 and Ru-doped In_2O_3. The optimized structures of substrate In_2O_3 (222), the modified Ru-doped In_2O_3 and the optimized structures of gas molecules adsorbed on the surface of materials are presented in Fig. S14.

The computed adsorption energy of TEA on the Ru-doped In_2O_3 surface was −3.95 eV, significantly higher than that on the pure In_2O_3 surface (−0.72 eV), indicating a markedly stronger interaction and enhanced gas-sensitive performance. In contrast, the absolute adsorption energies for interfering gases —including EtOH, acetone, hexane, and *n*-PrOH—were lower on the Ru-doped surface compared to the undoped counterpart (Fig. 5b). These results demonstrate a selective enhancement in TEA adsorption coupled with a suppression of interactions with other gas molecules.[51,52] The agreement between theoretical calculations and earlier experimental observations confirms that Ru incorporation effectively improves selectivity. According to the charge density difference maps (Fig. 5c), the charge transfer from TEA to Ru-In_2O_3 is 0.198*e*, which is bigger than that to pure In_2O_3 (0.162*e*), further consolidating the strong interactions between TEA and Ru-In_2O_3.[45,53,54]

Fig. 5d shows the density of states (DOS) of In_2O_3 and Ru-In_2O_3, where the vertical dashed line represents the Fermi level position. The band gap of Ru-doped In_2O_3 is narrowed, which is consistent with the experimental results of UV-vis spectroscopy (Fig. S12). As shown in Fig. 5e, the DOS curve is significantly shifted to the left after TEA gas adsorption, reflecting the change in conductivity before and after adsorption.[55,56] As mentioned above, DFT calculations suggest that Ru species introduction into In_2O_3 significantly enhances its adsorption energy for TEA, improves the electron transfer properties, and enhances the interaction with TEA for sensitive and selective sensing.

The main reasons for the improved sensitivity and selectivity of Ru-In_2O_3-0.8 compared to In_2O_3 can be ascribed to the following items (Fig. 5f): (i) The hollow microtubular structure with abundant pores on the walls would provide a high specific area and a large number of active sites for surface sensing reactions. This unique structure can facilitate penetration of more gas molecules into the inner region for subsequent sensing reactions. (ii) The formed Schottky potential barrier after incorporating Ru thickens the EDL, dramatically elevating the baseline resistance in air. The increased oxygen vacancies in Ru-In_2O_3-0.8 can offer more active sites to boost the surface sensing reaction. When exposed to TEA, the TEA molecules interact with the adsorbed oxygen ions on the material surface, releasing trapped electrons back into the conduction band, decreasing the resistance (R_g) to a large extent, thereby enlarging the difference between R_a and R_g. As a consequence, the gas response value is maximized. (iii) The high selectivity can be attributed to the preferential adsorption of TEA and its low bond dissociation energy. The bond dissociation energy of C–N in TEA is 307 kJ mol^{-1}, which is much lower than that of EtOH and *n*-PrOH (O–H, 458.8 kJ mol^{-1}), HCHO (C═O, 798.9 kJ mol^{-1}), and hexane (C–H, ∼400 kJ mol^{-1}; C–C, ∼360 kJ mol^{-1}).[23,24,57] The Ru species will promote the chemical reaction between active oxygen species and TEA molecules *via* catalytic effects.[58,59]

3.4. Seafood freshness monitoring demonstration

Stimulated by the improved sensing sensitivity and selectivity and the impressive low-concentration detection and stability, we fabricated a wireless TEA-sensing system for practical application. The sensing device coating with Ru-In_2O_3-0.8 as the sensing module was integrated with a local power, a microcontroller unit (MCU) and WiFi mode. This as-developed sensing system as a smart gas sensor with portable, lightweight and reliable handheld features was demonstrated for the real-time detection of the freshness of half-fin anchovy. The overall size is only 100 mm, 70 mm and 60 mm in three dimensions with an OLED display to show the monitored concentration of TEA. This monitoring process is also visual on a mobile phone *via* Wi-Fi technology. The outline and internal structure of the handheld device are shown in Fig. 6. Considering that aquatic products release complex volatile gases during meat spoilage with TEA as an important biomarker, we used a 0.8-Ru-In_2O_3 sensor to follow the spoilage process of 3 half-fin anchovies (weighing approximately 100 g) in a closed system (the experimental period was 24 hours).

The entire testing process was carried out in a sealed gas chamber with a volume of 20 L. During the monitoring process of the degree of food spoilage, we extracted 50 mL of gas from a beaker containing half-fin anchovies and injected it into the gas chamber after a certain period of time. Fig. 6f illustrates the relationship between the aging time for half-fin anchovy and the corresponding response values. It is evident that the response values exhibit an upward trend as spoilage progresses, reaching a response value of 16 at 24 hours (conc. = 483 ppb). This sensitive response characteristic can effectively capture the initial stage of fish spoilage. In Video S1, the spoilage extent of half-fin anchovies was assessed after 12 hours of storage. Upon injection of 50 mL of decay gas into the sealed chamber, the system enables online, real-time monitoring, with both the TEA concentration and the corresponding response value curve being simultaneously displayed on the mobile phone interface.

Furthermore, Fig. S15 illustrates the correlation between shrimp spoilage duration and Ru-In_2O_3-0.8 sensor response magnitude. The response values exhibit a continuous upward trend with progressive spoilage, reaching a peak of 106.9 at 168 hours (corresponding TEA concentration = 9.6 ppm) and demonstrating the universality of this sensor for monitoring

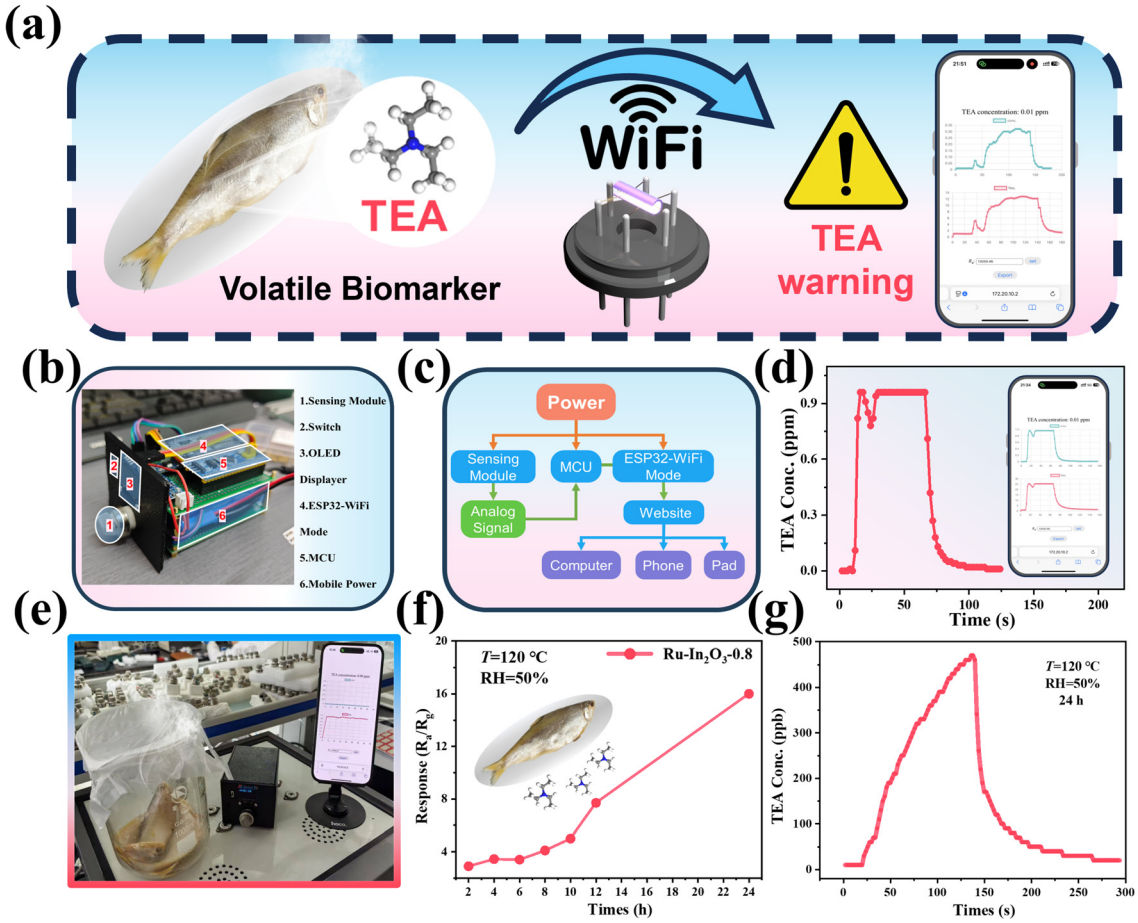

Fig. 6 (a) Schematic illustration of a smart TEA sensing system for monitoring fish freshness. (b) Image of the smart TEA sensor based on an STM32 microcontroller. (c) Logical diagram of the smart TEA sensing system. (d) Concentration curve of monitoring 1 ppm TEA gas on a smartphone. (e) Image of 100 g half-fin anchovy, a smart TEA sensing system and a smartphone. (f) Response values to the volatile biomarker TEA of half-fin anchovy spoiled for different periods at 120 °C under 50%RH. (g) TEA concentration curve of half-fin anchovy spoiled for 24 hours at 120 °C under 50%RH. All the relevant tests in this figure were conducted using the smart TEA sensing system, with data collection and real-time monitoring carried out using a smartphone.

the freshness of different types of seafood. The detailed testing conditions are presented in the SI. These observed results reveal that this smart gas sensing system could successfully capture the instantaneous TEA concentration variations, achieve the real-time monitoring of TEA, and ensure food freshness and safety.

4. Conclusion

This work demonstrates a Ru-In_2O_3 hollow hexagonal prism sensor with dual-enhanced sensitivity and selectivity for triethylamine (TEA) detection. The exceptional performance stems from a synergistic triple-mechanism design: (i) the hierarchical hollow structure facilitating gas diffusion and providing abundant active sites; (ii) Ru-induced Schottky barriers and oxygen vacancies that dramatically elevate baseline resistance (R_a), maximizing the response magnitude (R_a/R_g); and (iii) preferential TEA adsorption, its low C–N bond dissociation energy and Ru-catalyzed functions ensuring high selectivity. The sensing mechanism was further elucidated by theoretical calculations. The smart TEA sensing system enables real-time half-fin anchovy freshness monitoring, validating practical deployment potential. This work may expand the potential application of smart gas sensors in environmental contexts, food storage and transportation, and even noninvasive diagnosis by advanced sensing materials and sensing transducer optimization simultaneously.

Author contributions

X.-Z. S.: project administration, experimental design, data analysis, validation, and writing the manuscript. Y. X. C.: data curation, validation, and experimental design. J. T. Z.: methodology, validation, and investigation (wireless sensing system). D. K. L.: data curation and formal analysis. Z. W. L.: data curation, validation, and experimental design. Y. Y. W.:

data curation and formal analysis. Z. Z. N.: data curation and formal analysis. Y.-L. M.: formal analysis and discussion. F. L.: project administration, funding acquisition, and supervision. X.-F. W.: project administration, funding acquisition, and supervision. Z. Q. T.: project administration, funding acquisition, and supervision. All authors have approved the final manuscript.

Conflicts of interest

There are no conflicts to declare.

Data availability

The data supporting this article have been included as part of the supplementary information (SI). Supplementary information is available. Supplementary information is available, including additional experiments, structure characterizations, gas sensing data, structure mode in theoretical calculation and comparison table of gas sensing properties. See DOI: **https://doi.org/10.1039/d5qi02410b**.

Acknowledgements

The authors are grateful for the financial support from the National Natural Science Foundation of China (grant No. 22271036), the Natural Science Foundation of Liaoning Province of China (No. 2024-MSBA-17 and 2023-MSBA-012), the Fundamental Research Funds for the Central Universities of China (DUT24MS012 and DUT25Z2764), the Health Development Promotion Project – Spark Program Research Project (XHJH-0092), the Open Research Fund of Guangdong Advanced Carbon Materials Co., Ltd (Kargen-2024B0802) and Dalian Handisen Electronic Technology Co., Ltd.. This work is dedicated to Professor Zifeng Yan on the occassion of his 60th birthday.

References

1 S. Kim, Y. Kim, J. Kim, S. J. Kim, T. Kim, J. Sim, S. E. Jun, J. Lim, T. H. Eom, H. S. Lee, G. H. Lee, B. H. Hong, M. H. Oh, Y. S. Huh and H. W. Jang, Highly Selective Ammonia Detection in NiO–Functionalized Graphene Micropatterns for Beef Quality Monitoring, *Adv. Funct. Mater.*, 2024, **34**, 2407885.

2 M. Z. Ma, X. T. Yang, X. G. Ying, C. Shi, Z. X. Jia and B. C. Jia, Applications of Gas Sensing in Food Quality Detection: A Review, *Foods*, 2023, **12**, 3996.

3 N. F. D. Silva, C. M. R. Almeida, J. M. C. S. Magalhães, M. P. Gonçalves, C. Freire and C. Delerue-Matos, Development of a disposable paper-based potentiometric immunosensor for real-time detection of a foodborne pathogen, *Biosens. Bioelectron.*, 2019, **141**, 111317.

4 H. Zhang, Y. H. Guo and F. L. Meng, Metal Oxide Semiconductor Sensors for Triethylamine Detection: Sensing Performance and Improvements, *Chemosensors*, 2022, **10**, 231.

5 Y. Li, J. Sun, L. Huang, S. Liu, S. Wang, D. Zhang, M. Zhu and J. Wang, Nanozyme-encoded luminescent detection for food safety analysis: An overview of mechanisms and recent applications, *Compr. Rev. Food Sci. Food Saf.*, 2022, **21**, 5077–5108.

6 S. Liu, R. Shu, L. Huang, L. Dou, W. Zhang, Y. Li, J. Sun, M. Zhu, D. Zhang and J. Wang, Emergence of dyestuff chemistry-encoded signal tracers in immunochromatographic assays: Fundamentals and recent food applications, *Trends Food Sci. Technol.*, 2022, **127**, 335–351.

7 B. Zong, S. Wu, Y. Yang, Q. Li, T. Tao and S. Mao, Smart Gas Sensors: Recent Developments and Future Prospective, *Nano-Micro Lett.*, 2024, **17**, 54.

8 J. Bai, L. Xie, C. Chen, W. Yang, Z. Wei and Q. Zhang, In Situ PL Tracking the Evolution and Functionality of Oxygen Defects in the In_2O_3-Based NO_2 Gas Sensor, *ACS Sens.*, 2025, **10**, 8383–8394.

9 S. Wang, C. Tan, Q. Zong, S. Li, C. Gao, H. Yang, Q. Huang, P. French and H. Ye, Selective Reduction Laser Sintering: A New Strategy for NO_2 Gas Detection Based on In_2O_3 Nanoparticles, *Adv. Funct. Mater.*, 2025, **35**, 2419057.

10 Y. Yang, Y. He, S. Hu, Z. Li, L. Tan, M. Zhang, J. Xiong, Y. Hu, X. Wang, L. Fei, Z. Wang, H. Gu and J. Tang, Self-Embedded Schottky Junctions in Liquid-Metal-Derived 2D Oxides for Fast and Selective Room-Temperature H_2 Sensing, *Adv. Funct. Mater.*, 2025, **35**, 2500605.

11 S. M. Majhi, S. T. Navale, A. Mirzaei, H. W. Kim and S. S. Kim, Strategies to boost chemiresistive sensing performance of In_2O_3-based gas sensors: an overview, *Inorg. Chem. Front.*, 2023, **10**, 3428–3467.

12 Z. Sun, X. Yang, S. Yang, K. Li, X. Zhao, L. Yao, W. Xu, H. Wang, L. Guo and G. Pan, Ultrasensitive and ultra-selective room-temperature H_2S gas sensor based on CuO-loaded In_2O_3 2D porous nanosheets, *J. Hazard. Mater.*, 2025, **493**, 138355.

13 X. Yang, H. Fu, Y. Tian, Q. Xie, S. Xiong, D. Han, H. Zhang and X. An, Au decorated In_2O_3 hollow nanospheres: A novel sensing material toward amine, *Sens. Actuators, B*, 2019, **296**, 126696.

14 Y. Wang, B. Liu, D. Cai, H. Li, Y. Liu, D. Wang, L. Wang, Q. Li and T. Wang, Room-temperature hydrogen sensor based on grain-boundary controlled Pt decorated In_2O_3 nanocubes, *Sens. Actuators, B*, 2014, **201**, 351–359.

15 X. Wang, J. Su, H. Chen, G.-D. Li, Z. Shi, H. Zou and X. Zou, Ultrathin In_2O_3 Nanosheets with Uniform Mesopores for Highly Sensitive Nitric Oxide Detection, *ACS Appl. Mater. Interfaces*, 2017, **9**, 16335–16342.

16 S. Park, M. Kim, Y. Lim, D. Oh, J. Ahn, C. Park, S. Woo, W. Jung, J. Kim and I.-D. Kim, Dual-Photosensitizer Synergy Empowers Ambient Light Photoactivation of Indium Oxide for High-Performance NO_2 Sensing, *Adv. Mater.*, 2024, **36**, 2313731.

17 Z. Tao, Y. Li, B. Zhang, G. Sun, J. Cao and Y. Wang, Bi-doped urchin-like In_2O_3 hollow spheres: Synthesis and improved gas sensing and visible-light photocatalytic properties, *Sens. Actuators, B*, 2020, **321**, 128623.

18 Q. Yue, T. Liu, Y. Mu, X. T. Chen and X. T. Yin, Enhanced response for triethylamine detection by $NiCo_2O_4$-In_2O_3 composites gas sensor, *Chem. Eng. J.*, 2025, **509**, 161378.

19 J. He, Z. Cheng, Z. Liu, M. Yin, Y. Zhang, L. Han and Y. Xu, Epitaxial growth of Co_3O_4/In_2O_3 p-n heterostructure with rich oxygen vacancies for ultrahigh triethylamine sensing, *Sens. Actuators, B*, 2024, **400**, 134881.

20 D. Kong, B. Hong, J. Xu, X. Peng, J. Li, H. Chen, S. Qiu, N. Zhang and X. Wang, P–n heterojunction construction and interfacial interaction mechanism: NiO/In_2O_3 formaldehyde gas sensors with excellent sensitivity and selectivity, *Appl. Surf. Sci.*, 2025, **688**, 162442.

21 Y. Zhu, J. Wu, Z. Zhang, W. Wu, X. Wang, Y. Zhao and C. Zhao, PtCu Nanoparticles Sensitizing Mesoporous In_2O_3 Hexagonal Hollow Nanotubes for ppb-Level Formaldehyde Evaluation in Aquatic Products, *ACS Sens.*, 2025, **10**, 4348–4360.

22 D. H. Gao, Q. C. Yu, M. A. Kebeded, Y. Y. Zhuang, S. Huang, M. Z. Jiao and X. J. He, Advances in modification of metal and noble metal nanomaterials for metal oxide gas sensors: a review, *Rare Met.*, 2025, **44**, 1443–1496.

23 X. Qiao, D. Han, Z. Wang and F. Gu, Atomically dispersed Ru on three-dimensionally-ordered macroporous In_2O_3 for highly sensitive detection of triethylamine and the freshness of seafood, *Sens. Actuators, B*, 2024, **414**, 135943.

24 H. Sun, X. Tang, S. Li, Y. Yao and L. Liu, MOF-derived one-dimensional Ru/Mo co-doped Co_3O_4 hollow microtubes for high-performance triethylamine sensing, *Sens. Actuators, B*, 2023, **383**, 133583.

25 N. Luo, H. J. Cai, B. Lu, Z. G. Xue and J. Q. Xu, Pt-functionalized Amorphous RuO_x as Excellent Stability and High-activity Catalysts for Low Temperature MEMS Sensors, *Small*, 2023, **19**, 2300006.

26 N. Luo, C. Wang, D. Zhang, M. Guo, X. Wang, Z. Cheng and J. Xu, Ultralow detection limit MEMS hydrogen sensor based on SnO_2 with oxygen vacancies, *Sens. Actuators, B*, 2022, **354**, 130982.

27 W. Wei, N. Luo, X. Wang, Z. Xue, L. A. Shah, Q. Hu and J. Xu, Amorphous RhO_x decorated black indium oxide for rapid and flexible NO_2 detection at room temperature, *Sens. Actuators, B*, 2024, **414**, 135944.

28 X.-Z. Song, F.-F. Sun, S.-T. Dai, X. Lin, K.-M. Sun and X.-F. Wang, Hollow $NiFe_2O_4$ microspindles derived from Ni/Fe bimetallic MOFs for highly sensitive acetone sensing at low operating temperatures, *Inorg. Chem. Front.*, 2018, **5**, 1107–1114.

29 J.-H. Dong, X.-Z. Song, Y.-X. Chen, Z.-X. Gai, Z. Yuan, D.-K. Liu, Z. Tan, A. Liu, X.-F. Wang and S.-Y. Song, Engineering Ce Promoter to Regulate H^* Species to Boost Tandem Electrocatalytic Nitrate Reduction for Ammonia Synthesis, *Adv. Funct. Mater.*, 2025, **35**, 2422025.

30 D.-K. Liu, Y. Meng, Z. Gai, Y. Liu, Y. Wang, Z. Tian, X. Wang, Y. Wang, Z. Tan, L. Liu and X. Song, Dual-function Ln modification in multi-shell CoP: antioxidant stabilization and H^* adsorption modulation for boosting hydrogen evolution electrocatalysis, *Chem. Commun.*, 2025, **61**, 14189–14192.

31 X.-Z. Song, L. Qiao, K.-M. Sun, Z. Tan, W. Ma, X.-L. Kang, F.-F. Sun, T. Huang and X.-F. Wang, Triple-shelled ZnO/$ZnFe_2O_4$ heterojunctional hollow microspheres derived from Prussian Blue analogue as high-performance acetone sensors, *Sens. Actuators, B*, 2018, **256**, 374–382.

32 Z. Liu, Y. Wang, Y. Li, C. Sui, Y. Liu, Y. Liu, Y. Zhao, X. Liang, F. Liu and G. Lu, Bimetallic MOF derived mesoporous structure of Ru doped SnO_2 enable high-sensitivity gas sensors for triethylamine in high humidity, *Sens. Actuators, B*, 2024, **405**, 135275.

33 Y. Zhang, Y. Ma, Z. Wu, Z. Qin, H. Ji, X. Liu, W. Zhang and W. Hu, Abnormal p-type Gas-Sensing Response to Ether in Co-ZnO Nanocomposite Film and Its Significant Room-Temperature Magnetoresistance, *Adv. Funct. Mater.*, 2025, **35**, 2422705.

34 J. Li, E. Na, X. Liang, Q. Liang, M. Fan, H. Chen, G.-D. Li and X. Zou, Surface oxygen chemistry of metal oxide semiconductors for gas-sensing applications, *Inorg. Chem. Front.*, 2024, **11**, 8602–8626.

35 P. Song, F. Sun, T. Luan, Q. Meng and W. Geng, MOF-Derived In_2O_3/$BiVO_4$ Composites for Sensitive and Trace Detection of n-C_4H_9OH, *ACS Sens.*, 2025, **10**, 5589–5599.

36 M. Punginsang, A. Chaemsai, K. Inyawilert, M. Siriwalai, A. Wisitsoraat and C. Liewhiran, Performance and Selectivity toward Acetone against Various Gaseous Markers for Liver Diseases of Flame-Made Ir-Loaded In_2O_3 Nanoparticulate Sensors, *ACS Sens.*, 2025, **10**, 5748–5759.

37 F. Zhao, L. Yu, J. Wang, W. Cao, H. Zhang, H. Wang, P.-H. Wang and Z. Qiao, Metal–Organic Framework-Derived Au-Doped In_2O_3 Nanotubes for Monitoring CO at the ppb Level, *ACS Sens.*, 2024, **9**, 4007–4016.

38 M. Liu, A. Song, X. Zhang, J. Wang, Y. Fan, G. Wang, H. Tian, Z. Ma and G. Shao, Interfacial lithium-ion transportation in solid-state batteries: Challenges and prospects, *Nano Energy*, 2025, **136**, 110749.

39 J. Shao, C. Sun, H. Liu, P. He, Q. Liu, J. Sun, J. Li, G. Pan and X. Yang, Insight into Au functionalization on core-shell $LaFeO_3$ spheres for high-response and selectivity n-butanol gas sensors with DFT study, *Sens. Actuators, B*, 2023, **382**, 133506.

40 B. X. Feng, Z. Z. Wang, Y. Y. Feng, P. Li, Y. H. Zhu, Y. H. Deng, L. M. Wu, Q. Yue and J. Wei, Single-Atom Au-Functionalized Mesoporous SnO_2 Nanospheres for Ultrasensitive Detection of Biomarker at Low Temperatures, *ACS Nano*, 2024, **18**, 22888–22900.

41 X. Li, H. Hu, T. Tan, M. Sun, Y. Bao, Z. Huang, S. Muhammad, X. Xia and Y. Gao, Enhancing Methane Gas Sensing through Defect Engineering in Ag–Ru Co-doped

ZnO Nanorods, *ACS Appl. Mater. Interfaces*, 2024, **16**, 26395–26405.

42 M. Luo, X. Hu, Z. Fan, S. Ma, G. Song, L. Jin, C. Jie and S. Wang, Catalytic hydrogenation of CO_2 to formate by heterogenized Ru(III) catalyst and computational investigation of strong promoting effect with triethylamine, *Chem. Eng. J.*, 2023, **474**, 145622.

43 O. Wang, J. Kong, Z. Xue, B. An, J. Xu and X. Wang, Tailoring the Ni–O Microenvironment in Amorphous-Dominated Highly Active and Stable Zn/NiO for Hydrogen Sulfide Detection, *ACS Sens.*, 2024, **9**, 3233–3243.

44 W. Gao, X. Chang, O. Ola, Z. Wang, Q. Liao, X. Zhu, J. Li, Y. Jiang, D. Wang and S. Sun, Humidity-tolerant ammonia gas sensors based on $PrO_x/In_2O_3/WO_3$ heterostructure films, *Chem. Eng. J.*, 2025, **509**, 161482.

45 C. Li, D. Ma, S. Mou, Y. Luo, B. Ma, S. Lu, G. Cui, Q. Li, Q. Liu and X. Sun, Porous $LaFeO_3$ nanofiber with oxygen vacancies as an efficient electrocatalyst for N_2 conversion to NH_3 under ambient conditions, *J. Energy Chem.*, 2020, **50**, 402–408.

46 E. Na, S. Tao, W. Wang, J. Li, Y. Guo, R. Gao, Q. Li, F. Wang, C. Zhang and G.-D. Li, Ultrasensitive Acetone Gas Sensor Based on a K/Sn–Co_3O_4 Porous Microsphere for Noninvasive Diabetes Diagnosis, *ACS Sens.*, 2024, **9**, 6148–6156.

47 Y. Zhang, C. Zhang, Z. Zhang, H. Zong, P. Tan, L. Luo, Y. Luo and G. Duan, Double-Phase Ga-Doped In_2O_3 Nanospheres and Their Self-Assembled Monolayer Film for Ultrasensitive HCHO MEMS Gas Sensors, *Small*, 2025, **21**, 2411422.

48 X. Wang, H. Liang, B. Liu, Y. Meng, J. Ni, W. Sun, Y. Luan, Z. Tan and X.-Z. Song, Simultaneously Engineering Oxygen Defects and Heterojunction into Ho-Doped ZnO Nanoflowers for Enhancing n-Propanol Gas Detection, *Inorg. Chem.*, 2024, **63**, 12538–12547.

49 X.-B. Li, X. Hu, B. Yang, L.-H. Zheng, Y.-Y. Ren, F.-P. Wang, S. Sun, Y.-J. Wang, D.-N. Liu, H.-H. Xu, D.-W. Chen, W.-Q. Dang, Y.-X. Zhao and F.-R. Jin, Heterostructure engineering of $In_2O_3/ErVO_4$ hairy curd for high-performance TEA gas sensors, *Ceram. Int.*, 2024, **50**, 29590–29602.

50 B. Huang, S. Sun, X. Li, X. Li, N. Wang and X. Li, Layered $MoTe_2$/ZnO heterojunctions for sensitive TEA sensors at room temperature, *Sens. Actuators, B*, 2025, **439**, 137862.

51 Y. Li, Y. Li, Y. Shi, J. Gao, J. Lu, C. Wang, J. Chang, Z. Wang, Y. Yang, B. Yang, L. Feng, Q. Fu, X. Bao and Z.-S. Wu, Single cobalt atoms with unconventional dynamic coordination mechanism for selective ammonia sensor, *Natl. Sci. Rev.*, 2025, **12**, nwaf031.

52 Y. Liu, J. Guo, J. Wang, Y. Zhang, G. Gu, H. Ruan, P. Li, Y. Sun, L. Zhang, W. Liu, Z. Du and G. Cheng, Triboelectric plasma regulated ZnO thin films for ultra-low power room-temperature acetone gas sensing, *Nano Energy*, 2025, **145**, 111430.

53 Y. F. Zhan, J. Poisson, X. T. Meng, Z. B. Wang, L. Z. Chen, T. H. Wu, R. Koehler and K. Zhang, Electrospun Lignin/ZnO Nanofibrous Membranes for Self-Powered Ultrasensitive Flexible Airflow Sensor and Wearable Device, *Adv. Mater.*, 2025, **37**, e2502211.

54 L. X. Xue, J. H. Cui, R. Y. Li, W. H. Xie, K. Y. Chen, H. X. Yu, L. M. Wu, T. J. Ni, Q. Yue and Y. H. Deng, Interface Engineering p-n Heterostructured Core-Shell Mesoporous Particles for Cascade Catalysis Promoted Gas Sensing, *Adv. Mater.*, 2025, **37**, e2416006.

55 J. Lee, M. Kim, S. Park, J. Lee, Q. Chen, J. Kim, T. Defferriere, H. Park, S. Jeon and I.-D. Kim, Bandgap-Engineered Graphene Quantum Dot Photosensitizers for Tunable Light Spectrum-Activated NO_2 Sensors, *ACS Nano*, 2025, **19**, 32732–32743.

56 H. Lee, J.-S. Lee, G.-W. Kwak, J. Kim, K.-M. Kim, D. G. Kang, G.-N. Yun, H.-T. Kim, S.-J. Choi and S.-J. Kim, Carbide-Induced Thermal Shock Synthesis of High-Entropy Alloy Nanoparticles Anchored on WO_3 Nanofibers for High-Performance Gas Sensors, *ACS Nano*, 2025, **19**, 18095–18107.

57 X. Tan, X. Chen, J. Guo, L. Wang, Z. Dong, X. Li, L. Yang, D. Zhang, L. Qian and C. He, High performance and highly selective sensing of triethylamine sensors based on Cu-doped MoO_3 nanobelts, *J. Alloys Compd.*, 2024, **976**, 173152.

58 R. X. Qin, L. Y. Zhou, P. X. Liu, Y. Gong, K. L. Liu, C. F. Xu, Y. Zhao, L. Gu, G. Fu and N. F. Zheng, Alkali ions secure hydrides for catalytic hydrogenation, *Nat. Catal.*, 2020, **3**, 703–709.

59 Y. Tang, Y. Wu, W. Xu, L. Jiao, Y. Chen, M. Sha, H.-R. Ye, W. Gu and C. Zhu, Ultrathin Ruthenium Nanosheets with Crystallinity-Modulated Peroxidase-like Activity for Protein Discrimination, *Anal. Chem.*, 2021, **94**, 1022–1028.

